

1 **The Role of Chemical Boundary Conditions in Simulating Summer Ozone and**
2 **Cross-Boundary Transport over China**

3
4
5 Yunsong Du^{1,2}, Fumo Yang¹, Sijia Lou³, Baolei Lyu⁴, Ran Huang⁵, Guangming Shi¹,
6 Yongtao Hu⁶, Yan Jiang⁷, Nan Wang^{1*}

7
8
9
10 ¹College of carbon Neutrality Future Technology, Sichuan University, Chengdu 610065, China

11 ²Department of Environmental Science and Engineering, Sichuan University, Chengdu 610065,
12 China

13 ³School of Atmospheric Sciences, Nanjing University, Nanjing 210023, China

14 ⁴Huayun Sounding Meteorological Technology Co. Ltd., Beijing 100081, China

15 ⁵Hangzhou AiMa Technologies, Hangzhou, Zhejiang 311121, China

16 ⁶School of Civil and Environmental Engineering, Georgia Institute of Technology, Atlanta,
17 Georgia 30332, USA

18 ⁷ Sichuan Eco-environment Monitoring Station, Chengdu 610091, China

19
20 ***Correspondence:** Nan WANG (nan.wang@scu.edu.cn)

21

22 **Key Points**

- 23 1. We systematically evaluated the impacts of chemical boundary conditions (static vs.
24 dynamic) on regional O₃ simulations over China.
- 25 2. Chemical boundary conditions strongly modulate O₃ simulations via cross-
26 boundary transport in both horizontal and vertical directions.
- 27 3. Synoptic circulation dynamically amplifies the impacts of chemical boundary
28 conditions on regional O₃ levels.

29

30

31 **Abstract**

32 Regional chemical transport models are vital for diagnosing and forecasting
33 tropospheric ozone (O₃) pollution. However, their accuracy is often limited by the
34 simplified treatment of chemical boundary condition (CBC). This study provides a
35 comprehensive evaluation of how different CBC influence regional O₃ simulations over
36 China using the WRF–CMAQ model. Four CBC scenarios were assessed: a static
37 BASE profile representing climatological conditions and three dynamic scenarios
38 derived from H-CMAQ, GEOS-Chem, and CESM2.2. Model results were validated
39 with surface networks, ozonesonde profiles, and satellite O₃ columns. The BASE
40 scenario underestimated the average maximum daily 8-hour O₃ (avg-O₃MDA8) and its
41 90th percentile by –5.7% and –13.1%, respectively, while dynamic CBC substantially
42 improved the accuracy. GEOS-Chem achieved the lowest bias (–0.3%) and highest
43 agreement (IOA = 0.85 and 0.83) for avg-O₃MDA8 and its 90th percentile. H-CMAQ
44 performed best in high-elevation northwestern regions, and CESM2.2 excelled in
45 southern and southwestern areas. Vertically, all CBC reasonably matched observations
46 within the troposphere, but elevated lower-stratosphere biases were identified in BASE,
47 H-CMAQ, and CESM2.2. A case study contrasting cyclone-scavenging and post-trough
48 accumulation phases revealed that dynamic CBC enhance cross-boundary transport
49 efficiency, raising O₃ by 10–20% over eastern China through combined continental and
50 stratospheric inflows. These results underscore the crucial role of synoptic circulation–
51 driven transboundary transport in shaping regional O₃ concentrations and demonstrate
52 the importance of realistic, time-varying CBC for improving regional O₃ simulations,
53 air quality forecasting, and transboundary pollution management in China.

54

55 **Key words:** O₃ simulation; cross-boundary transport; chemical boundary condition;
56 chemical transport model

57

58 **1 Introduction**

59 Ozone (O₃) pollution is a critical environmental issue with profound implications for
60 air quality (Malley et al., 2017; Chiu et al., 2023). As a secondary pollutant,
61 tropospheric O₃ is mainly formed through photochemical reactions involving
62 precursors such as nitrogen oxides (NO_x) and volatile organic compounds (VOCs)
63 under sunlight. Elevated O₃ concentrations pose severe risks to public health,
64 contributing to respiratory diseases and premature mortality, while also damaging
65 ecosystems and suppressing agricultural productivity (WHO, 2016; Wang et al., 2017;
66 Zhang et al., 2019a). In addition, as a highly reactive oxidant, tropospheric O₃ regulates
67 the atmospheric lifetime of numerous reactive trace gases by governing their chemical
68 transformations (Jacob, 2003).

69 O₃ pollution is currently one of the most pressing environmental challenges faced
70 globally. In many Western countries, stringent air pollution controls implemented since
71 the last century have led to stabilization or even declines in O₃ concentrations (Monks
72 et al., 2015; Tarasick et al., 2019). Over the past decades, China has experienced
73 frequent high-ozone episodes, drawing increasing attention from both the scientific
74 community and policymakers. Even though, China has only more recently undertaken
75 aggressive air quality improvement measures, most notably through the Air Pollution
76 Prevention and Control Action Plan launched in 2012, which mandated substantial
77 reductions in nitrogen oxide emissions. Despite these efforts, O₃ concentrations in
78 China have not shown a sustained decline; instead, they have continued to rise in major
79 urban agglomerations such as the North China Plain and the Yangtze River Delta
80 (Zhang et al., 2019b; Lu et al., 2020; Wang et al., 2020; Wang et al., 2022). Nevertheless,
81 the formation and distribution of O₃ are governed by the interplay of precursor
82 emissions, meteorology, and transport processes. Variations in the magnitude and
83 composition of anthropogenic and natural NO_x and VOC emissions shape the chemical
84 regime for O₃ production and loss. Meteorological conditions (e.g., temperature, solar
85 radiation, humidity, boundary layer dynamics, and circulation patterns) further
86 modulate photochemical reaction rates, vertical mixing, and horizontal transport, while
87 surface characteristics and complex topography can influence local stagnation and
88 recirculation. Together with regional and transboundary transport, as well as inflow
89 from the free troposphere and occasional stratosphere–troposphere exchange, these
90 processes determine background O₃ levels and lead to strong spatial and seasonal
91 heterogeneity in O₃ pollution (Monks et al., 2015; Lu et al., 2018). Regional chemical
92 transport models (CTMs) are essential tools for predicting and diagnosing air pollution,
93 particularly photochemical O₃ pollution. Unlike global models, which emphasize large-
94 scale atmospheric processes at coarse spatial resolutions, regional models such as the
95 Community Multiscale Air Quality (CMAQ) and the Weather Research and Forecasting
96 model with Chemistry (WRF-Chem) resolve chemical and physical processes at finer
97 spatial and temporal scales (Byun and Schere, 2006; Grell et al., 2005). This capability
98 enables them to capture the complex interactions among local emissions, meteorology,
99 and topography that govern the formation, transport, and dispersion of O₃ and its
100 precursors. However, the reliability of CTM-based O₃ simulations ultimately depends
101 on the accuracy and consistency of the meteorological fields, emission inputs, and

102 chemical boundary conditions that define the model environment (Hogrefe et al., 2018;
103 Solazzo et al., 2012).

104 Over the past decade, CTMs have become central to air quality forecasting, scientific
105 research, environmental assessment and policy evaluation (Yahya et al., 2015; Bai et
106 al., 2018; Wang et al., 2021b; Gao et al., 2024). Their flexible domain configurations
107 allow targeted simulations over regions with intense emissions or complex terrain, such
108 as urban agglomerations and mountainous areas (Wang et al., 2019; Mao et al., 2022a;
109 Dou et al., 2024). Besides, incorporating high-resolution emission inventories and
110 region-specific meteorological inputs further enhances their accuracy. Numerous
111 applications have demonstrated their scientific and practical value: Zhang et al. (2019b)
112 used WRF-CMAQ to disentangle the relative roles of anthropogenic emissions and
113 meteorology in PM_{2.5} variability, while Mao et al. (2022a) reproduced multi-pollutant
114 trends across China between 2013 and 2019, validating CMAQ's long-term
115 performance. Wang et al. (2024) applied CMAQ to assess regional O₃ responses during
116 heatwaves, highlighting the strong sensitivity of O₃ formation to both emissions and
117 meteorological drivers. Collectively, these applications underscore the indispensable
118 role of regional CTMs in advancing mechanistic understanding of air pollution and in
119 guiding effective clean-air strategies (Yahya et al., 2015; Lei et al., 2023; Dou et al.,
120 2024; Geng et al., 2024).

121 Building on this foundation, substantial efforts have focused on improving the
122 performance and reliability of regional CTMs. A major area of optimization lies in
123 chemical mechanisms: updated frameworks such as Carbon Bond 6 (CB6) and SAPRC-
124 11 enhance model fidelity in representing O₃ formation pathways and secondary organic
125 aerosol production under diverse atmospheric conditions (Yarwood et al., 2010; Carter
126 and Heo, 2013). Parallel improvements in meteorological simulations—through
127 techniques such as four-dimensional data assimilation (FDDA) in WRF and the
128 incorporation of high-resolution land-use datasets (e.g., MODIS, NLCD)—have
129 sharpened the representation of surface temperature, planetary boundary layer height,
130 and wind fields (Mallard et al., 2018; Campbell et al., 2019; Godowitch et al., 2015;
131 Wang et al., 2021a; Siewert and Kroszczyński, 2023). Meanwhile, advances in
132 anthropogenic and biogenic emission inventories, including the Multi-resolution
133 Emission Inventory for China (MEIC) and the U.S. National Emissions Inventory (NEI),
134 now provide finer spatial and temporal detail, capturing sector-specific variability and
135 reducing input uncertainty (Li et al., 2017a; Zheng et al., 2021; Foley et al., 2023; Geng
136 et al., 2024). Together, these continuous advancements have considerably strengthened
137 the capacity of regional CTMs to support both scientific inquiry and evidence-based
138 policy-making.

139 Despite substantial advances in regional chemical transport models (CTMs),
140 comparatively little attention has been devoted to chemical boundary conditions (CBC),
141 even though they critically influence model accuracy. CBC specify the concentrations
142 of air pollutants at the lateral and vertical boundaries of the simulation domain, thereby
143 constraining internal chemical evolution and pollutant transport (Goldberg et al., 2015;
144 Hogrefe et al., 2018). Accurate CBC are essential for capturing the impact of long-range
145 pollutant transport and representing background concentrations, both of which strongly

146 shape regional air quality. For regional O₃, these boundary-driven background levels
147 can modulate the effectiveness of local emission controls, alter the chemical sensitivity
148 regime, and partly determine the spatial gradients between upwind and downwind areas.
149 In regions strongly influenced by continental outflow, stratosphere–troposphere
150 exchange, or marine inflow, poorly specified CBC may therefore lead to systematic
151 biases in simulated O₃ distributions (Zhu et al., 2024; Goldberg et al., 2015; Hogrefe et
152 al., 2018). Oversimplified treatments—such as prescribing fixed background values or
153 climatological means—can introduce substantial biases, resulting in misrepresentation
154 of pollutant levels and misleading evaluations of source contributions, policy
155 effectiveness, and health risks (Yahya et al., 2015; Hogrefe et al., 2018). Indeed,
156 sensitivity studies show that uncertainties in CBC can alter simulated O₃ by several
157 parts per billion, with particularly pronounced effects in downwind and coastal regions
158 influenced by transboundary transport (Hogrefe et al., 2018; Jerrett et al., 2005) .
159 In China, few studies have systematically assessed the role of chemical boundary
160 conditions in influencing model performance or pollutant attribution across different
161 geographical regions (Zhu et al., 2024). This represents a critical gap, as the spatial
162 heterogeneity of transboundary influences—from continental transport in the west to
163 marine outflow in the east—could lead to regionally differentiated impacts on pollutant
164 concentrations and control policy outcomes. For example, western and northern China
165 may be more strongly affected by inflow of polluted air masses from upwind continental
166 source regions, while eastern coastal areas can be influenced by recirculation and clean
167 or polluted marine air, leading to distinct baseline O₃ levels and vertical structures.
168 Without an explicit assessment of CBC across these contrasting regimes, regional CTM
169 applications may under- or overestimate O₃ burdens and misattribute observed spatial
170 patterns to local emissions or meteorology alone (Solazzo et al., 2012; Ni et al., 2018;
171 Sahu et al., 2021; Mao et al., 2022b; Shen et al., 2024). Therefore, a comprehensive
172 evaluation of the role of chemical boundary conditions in regional CTM applications is
173 urgently needed to enhance model reliability, reduce forecast uncertainty, and support
174 the formulation of more effective O₃ mitigation strategies.
175 Herein, we used outputs from three global chemical transport models to provide
176 downscaled CBC for the regional CMAQ model and systematically evaluated the
177 impact of including versus omitting CBC on O₃ simulations. Surface observations,
178 ozonesonde profiles, and satellite data were used to assess model performance across
179 China. We also examine the mechanisms by which CBC influence O₃, including their
180 regulation of background concentrations and propagation of transboundary pollutants
181 into the domain. This study advances understanding of CBC in regional air quality
182 modeling and provides a foundation for more accurate high-resolution O₃ forecasts and
183 improved air quality management strategies. By explicitly contrasting simulations with
184 and without chemically consistent CBC, while keeping emissions and meteorology
185 unchanged, this study isolates the contribution of boundary conditions from other key
186 drivers of O₃ variability. The resulting diagnostics provide a clearer physical
187 interpretation of how CBC interact with regional emissions and meteorological fields
188 to shape O₃ distributions over China.

189

190 **2 Data and Method**

191 **2.1 Modelling Configuration**

192 In this study, O₃ concentrations during July–August 2019 were simulated using the
193 WRF-CMAQ modeling system. The Weather Research and Forecasting (WRF,
194 <https://www.mmm.ucar.edu/models/wrf>) model version 3.9.1 was used to generate
195 meteorological fields, which were then provided as inputs to drive the Community
196 Multiscale Air Quality (CMAQ) model version 5.3.3 (<http://www.epa.gov/cmaq>).
197 CMAQ solves the governing physical and chemical equations to simulate the three-
198 dimensional distribution of air pollutants. The simulations were conducted at a
199 horizontal resolution of 36 km, covering the entire Chinese mainland and surrounding
200 regions to ensure adequate representation of regional transport processes (see Fig. 1).
201 The meteorological initial and boundary conditions were derived from the ERA5
202 reanalysis dataset (0.25° × 0.25° resolution), provided by the Copernicus Climate
203 Change Service via the Climate Data Store (CDS) (Hersbach et al., 2023).
204 Anthropogenic emissions over China were obtained from the Multi-resolution Emission
205 Inventory for China (MEIC v1.4) for the year 2019 (Li et al., 2017a), which provides
206 sector-based emissions mapped to CMAQ species (<http://meicmodel.org>, last accessed:
207 January 1, 2024). For regions outside China, anthropogenic emissions were based on
208 the MIX v1.1 inventory (Li et al., 2017b). This dataset provides monthly grid-based
209 emission data at a 0.25° spatial resolution across five key sectors (power, industry,
210 residential, transport, and agriculture), meeting the requirements for multi-scale
211 atmospheric chemical transport modeling (<http://meicmodel.org.cn>, last access:13 Apr.
212 2026). The biogenic emissions were estimated using the inline Biogenic Emission
213 Inventory System (BEIS3) embedded within CMAQ which dynamically calculates
214 emissions based on land use, vegetation type, and meteorological conditions online.
215 The gas-phase chemistry was represented using the SAPRC07TC mechanism, while
216 aerosol processes were simulated using the AERO6 module.

217 In order to assess the influence of CBC on O₃, four different CBC scenarios were
218 designed and applied as inputs to the CMAQ BCON (boundary condition) module. The
219 first scenario, referred to as BASE, employs a spatially uniform and temporally constant
220 boundary condition derived from the built-in ASCII vertical profiles in CMAQ. These
221 profiles were extracted from a hemispheric CMAQv5.3 beta2 simulation for the year
222 2016, representing annual mean concentrations at the grid cell nearest to (37N, -157W),
223 which is over the ocean in the central North Pacific region. Therefore, the BASE CBC
224 represent the background profile of the open ocean environment. In contrast, the
225 remaining three scenarios utilize boundary conditions generated from the output of
226 three global chemistry models (GCMs), namely, Hemisphere version of the Community
227 Multiscale Air Quality model (H-CMAQ), Goddard Earth Observing System-
228 Chemistry (GEOS-Chem), and Community Earth System Model version 2.2
229 (CESM2.2). Each of these boundary datasets was processed and formatted consistently
230 to ensure compatibility with the CMAQ framework.

231 Specifically, CBC for the H-CMAQ scenario were derived from daily averaged species
232 concentration outputs produced by a hemispheric CMAQ simulation under the U.S.
233 EPA's Air Quality Time Series (EQUATES) Project
234 (<http://www.epa.gov/cmaq/EQUATES>, last accessed: 1 August 2024). These
235 simulations were conducted using a customized version of CMAQ v5.3.2, with a

236 horizontal resolution of 108×108 km on a polar stereographic projection, and
237 employed the CB6R3M_AE7_KMTBR chemical mechanism.

238 For the GEOS-Chem scenario, 3-hourly global simulation outputs were used. The
239 GEOS-Chem model is a global 3-D chemical transport model driven by meteorological
240 fields from NASA's Goddard Earth Observing System (GEOS), developed by the
241 NASA Global Modeling and Assimilation Office. The chemical mechanism includes
242 comprehensive tropospheric O_3 - NO_x -VOCs-aerosol-halogen chemistry (Mao et al.,
243 2013; Park et al., 2004; Parrella et al., 2012; Wang et al., 1998), as well as stratospheric
244 chemistry processes (Eastham et al., 2014). Further information is available at
245 <https://geoschem.github.io/> (last accessed: 1 August 2024).

246 The CESM2.2 scenario utilized 6-hourly output from the Community Atmosphere
247 Model with Chemistry (CAM-chem) embedded within the Community Earth System
248 Model version 2.2 (CESM2.2). The CAM-chem simulations used the finite-volume
249 dynamical core, with a horizontal resolution of $1^\circ \times 1^\circ$ and 32 vertical levels. The
250 MOZART-T1 mechanism was applied to simulate both tropospheric and stratospheric
251 chemical processes. Details on the model setup and outputs are available at
252 <https://www2.acom.ucar.edu/gcm/cam-chem> (last accessed: 1 August 2024).

253 All three global model outputs were converted to the I/O API format required by the
254 CMAQ Chemical Transport Model (CCTM). A combination of data transformation
255 tools and custom scripts was developed and applied to harmonize species mapping,
256 spatial resolution, temporal alignment, and file formatting, thus enabling seamless
257 integration of each global model dataset as boundary conditions for the regional CMAQ
258 simulations. To minimize the influence of initial conditions and allow the imposed
259 boundary conditions to fully propagate throughout the simulation domain, a 10-day
260 model spin-up period was applied prior to the analysis period.

261

262 2.2 Observation data

263 2.2.1 Surface observation data

264 Surface observations across China for July–August 2019 were used to evaluate the
265 simulated meteorological parameters and atmospheric pollutant concentrations from
266 the WRF-CMAQ model. Meteorological data were obtained from the National
267 Meteorological Information Center (<http://data.cma.cn>, last accessed 1 January 2024).
268 Hourly meteorological observations from 2,394 monitoring stations were collected,
269 including 2-meter air temperature (T2), 2-meter relative humidity (RH2), 10-meter
270 wind speed (WS10), and surface pressure (PRS). Hourly O₃ observations were retrieved
271 from the China National Environmental Monitoring Center
272 (<https://air.cnemc.cn:18007/>, last accessed 1 January 2024), encompassing data from
273 1,480 air quality monitoring sites. The spatial distribution of meteorological and air
274 quality monitoring stations is shown in Fig. 1 and Fig. S1. To investigate the spatial
275 variability of chemical boundary condition impacts on O₃ simulation, monitoring sites
276 were grouped into seven regions within China (Fig. 1 and Table S1): South (S), East
277 (E), North (N), Central (C), Northeast (NE), Northwest (NW), and Southwest (SW).
278 This study evaluates sites O₃ using the Maximum Daily 8-Hour Average concentration
279 (O3MDA8), derived from both surface observations and model simulations. To
280 comprehensively assess model performance across different pollution levels, we
281 analyze two key indicators: the average O3MDA8 (avg-O3MDA8), which reflects the
282 overall background and typical exposure level, and the 90th percentile of O3MDA8
283 (90th-O3MDA8), which is used to characterize high-O₃ events. The inclusion of the
284 90th percentile metric enables evaluation of the model’s ability to capture peak O₃
285 pollution episodes that are most relevant to regulatory thresholds and public health risk
286 assessments.

287 Model performance was quantitatively evaluated using multiple statistical metrics,
288 including mean observed value (OBS), mean simulated value (SIM) for each of the four
289 CBC scenarios (BASE, H-CMAQ, GEOS-Chem, CESM2.2), mean bias (MB),
290 normalized mean bias (NMB), root mean square error (RMSE), index of agreement
291 (IOA), and Pearson correlation coefficient (r). The IOA ranges from 0 to 1, where 1
292 indicates a perfect match between simulated and observed values, while values
293 approaching 0 indicate poor model performance (Willmott, 1981). The mathematical
294 definitions of these statistics are provided below.

$$295 \quad \text{OBS} = \frac{1}{n} \sum_{i=1}^n O_i$$

$$296 \quad \text{SIM} = \frac{1}{n} \sum_{i=1}^n S_i$$

$$297 \quad \text{MB} = \frac{1}{n} \sum_{i=1}^n (S_i - O_i)$$

$$298 \quad \text{NMB} = \frac{\sum_{i=1}^n (S_i - O_i)}{\sum_{i=1}^n O_i}$$

$$299 \quad \text{RMSE} = \sqrt{\frac{1}{n} \sum_{i=1}^n (S_i - O_i)^2}$$

$$300 \quad r = \frac{\sum_{i=1}^n (S_i - \text{SIM})(O_i - \text{OBS})}{\sqrt{\sum_{i=1}^n (S_i - \text{SIM})^2} \sqrt{\sum_{i=1}^n (O_i - \text{OBS})^2}}$$

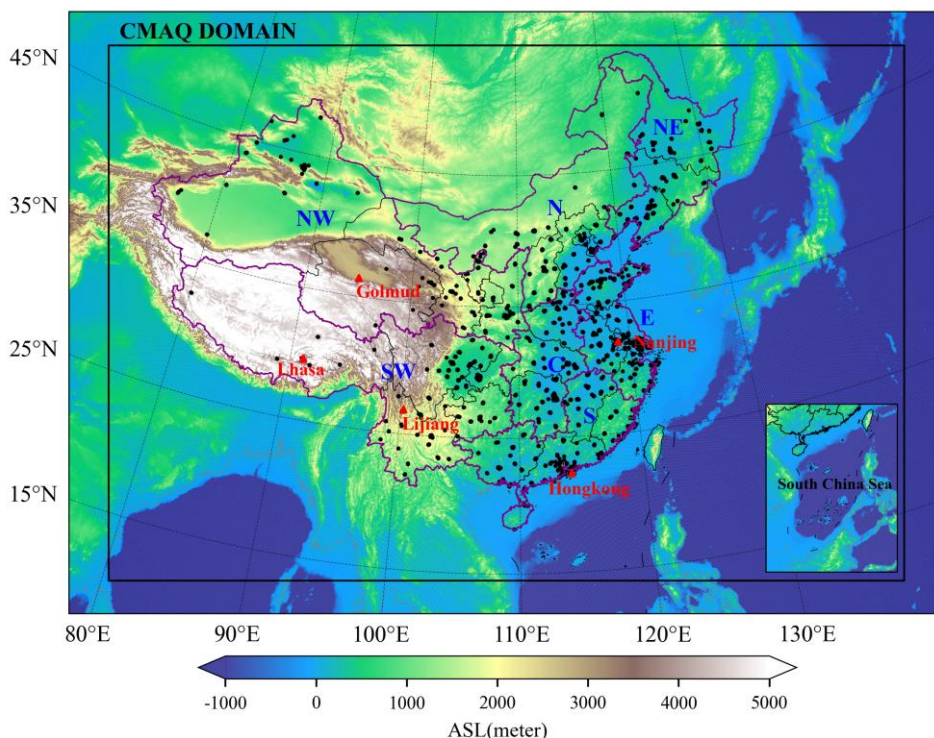
$$301 \quad \text{IOA} = 1 - \frac{n * \text{RMSE}^2}{\sum_{i=1}^n (|S_i - \text{OBS}| + |O_i - \text{OBS}|)^2}$$

302 where S_i and O_i are the simulated and observed site's avg-O3MDA8 or 90th-
303 O3MDA8, n represents the number of the simulated days.

304 2.2.2 Vertical Observation Data

305 To evaluate the influence of CBC on the vertical distribution of O_3 , O_3 sounding data
306 from five representative sites (Hong Kong, Nanjing, Golmud, Lhasa, and Lijiang) were
307 collected and used to validate the model's vertical O_3 simulations. These stations are
308 strategically located in the eastern, southern, southwestern, and northwestern
309 boundaries of the modeling domain (Fig 1), enabling a targeted assessment of how
310 boundary conditions affect O_3 concentrations aloft. Briefly, the Hong Kong profiles
311 (King's Park Observatory; launched at 13:00 LST; 9 soundings during July–August
312 2019) were obtained from the World Ozone and Ultraviolet Radiation Data Centre
313 (WOUDC, <https://woudc.org/data.php>, last accessed: October 8, 2024). Nanjing
314 observations (from the National Benchmark Climate Station; launched between 13:00
315 and 14:00 LST; 4 soundings between July 23, 2019 and September 1, 2020) were
316 sourced from the China Air Pollution Data Center (CAPDC,
317 <https://www.capdatabase.cn>, last accessed: October 8, 2024). Data for Golmud (12
318 profiles), Lhasa (8 profiles), and Lijiang (5 profiles), collected between 2019 and 2022
319 with launch times ranging from 23:00 to 02:00 LST, were obtained from the National
320 Tibetan Plateau Data Center (TPDC, <https://data.tpdc.ac.cn/home>, last accessed:
321 October 10, 2024) (Bai Zhixuan, 2023; Zhixuan, 2023; Bai Zhixuan, 2022). To ensure
322 consistency across datasets and comparability with the model output, all sonde data
323 were processed for the 0–20 km height above ground level (HAGL) range and
324 interpolated to match the model vertical structure, and data within the 0–16 km HAGL
325 layer were used in the model evaluation. Observations during July–August were
326 prioritized, and model outputs were extracted as time-averaged vertical profiles over
327 the corresponding grid cells and times (13:00 -14:00 or 23:00 - 2:00 LST). Detailed
328 information about the surface observation and sounding sites is provided in Table S2.
329 In addition, tropospheric O_3 column data were also introduced to further evaluate the
330 spatial performance of the model. This dataset was developed by the University of
331 Science and Technology of China (USTC) and is derived from measurements by the
332 Environmental Trace Gases Monitoring Instrument (EMI) aboard the Gaofen-5 satellite,
333 China's first ultraviolet-visible hyperspectral spectrometer dedicated to atmospheric
334 composition monitoring. The product provides a seamless tropospheric O_3 column

335 dataset at a high spatial resolution of $1 \text{ km} \times 1 \text{ km}$, offering detailed information on O_3
 336 distribution over complex terrains and urban regions. Further details on the retrieval
 337 algorithm and validation of the product can be found in (Zhao et al., 2024). Detailed
 338 information about the tropospheric O_3 column data is also provided in Table S2.
 339



340
 341 **Figure 1.** Simulation domain of the CMAQ model with a horizontal resolution of $36 \times 36 \text{ km}^2$. Black
 342 dots represent surface O_3 monitoring sites, and red triangles denote O_3 sounding launch stations.
 343 Terrain elevation above sea level (ASL) is illustrated with shaded relief. Purple lines delineate the
 344 administrative boundaries of China's major regions—South (S), East (E), North (N), Central (C),
 345 Northeast (NE), Northwest (NW), and Southwest (SW). The provinces included in each region are listed
 346 in Table S1.

347 **3. Results and Discussions**

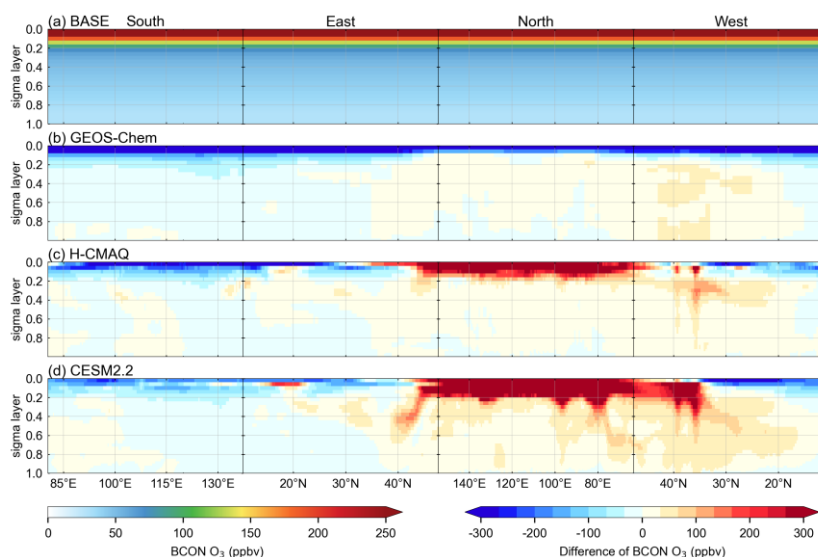
348 **3.1 Comparative Analysis of four CBC**

349 Figure 2 displays the vertically averaged temporal O_3 distribution along the four lateral
 350 boundaries of the modelling domain during July-August 2019, under four different
 351 CBC scenarios. In the BASE scenario, the O_3 profile remains static, characterized by
 352 horizontally uniform mixing ratios at each altitude. A sharp increase in O_3 concentration
 353 is evident near the tropopause, with minimal vertical variation in the lower and mid-
 354 troposphere. This relatively uniform, three-dimensional O_3 distribution suggests that
 355 the BASE CBC scenario represents a background condition (i.e., over the open ocean),
 356 and thus fails to adequately capture the spatiotemporal variability of O_3 over mainland
 357 East Asia, where O_3 levels are strongly influenced by anthropogenic emissions and
 358 regional transport processes.

359 In contrast to the static pattern in the BASE scenario, the O_3 boundary conditions

360 extracted from the three global models (H-CMAQ, GEOS-Chem, and CESM2.2)
 361 exhibit both horizontal and vertical variability across the four lateral boundaries. These
 362 three scenarios display a generally consistent spatial and vertical structure. However,
 363 notable differences still exist across different boundaries. In the lower troposphere (0–
 364 3 km), the average O₃ concentrations from the three global models are 5–7 ppbv lower
 365 than those in the BASE scenario along the southern and eastern boundaries, with only
 366 minor differences among the models. For instance, over the oceanic portions of these
 367 boundaries, specifically the eastern segment of the southern boundary and the southern
 368 segment of the eastern boundary, the BASE scenario overestimates boundary O₃
 369 concentrations by as much as 20–30 ppbv. In contrast, along the northern and western
 370 boundaries, the global models generally produce 4–20 ppbv higher O₃ concentrations
 371 than the BASE scenario, accompanied by greater inter-model variability. Among them,
 372 H-CMAQ and GEOS-Chem show relatively similar patterns, whereas CESM2.2
 373 exhibits substantially higher O₃ levels, particularly along the western boundary (Fig. 2
 374 and Table 1).

375 Conversely, compared to the BASE scenario, the differences in boundary O₃
 376 concentrations among the three global models significantly increase in the mid-to-upper
 377 troposphere (3–10 km) and stratosphere (above 10 km). In the mid-to-upper troposphere
 378 (3–10 km), the BASE scenario generally underestimates O₃ concentrations along the
 379 northern and western boundaries, while significantly overestimates them along the
 380 southern boundary. The CESM2.2 scenario shows higher O₃ concentrations along the
 381 eastern, northern, and western boundaries. In the stratosphere (above 10 km), the global
 382 model results indicate that the BASE scenario significantly overestimates O₃
 383 concentrations along the southern, eastern, and western boundaries, with GEOS-Chem
 384 exhibiting the lowest O₃ concentrations among the four scenarios. The H-CMAQ and
 385 CESM2.2 models show large areas of high O₃ concentration near the northern boundary.
 386 These spatial variations in O₃ boundary conditions are likely to have a considerable
 387 impact on the simulation of surface O₃ concentrations over China during the summer
 388 months.



389

390 **Figure 2.** Temporally averaged O₃ chemical boundary conditions along the lateral boundaries of the

391 CMAQ modeling domain. Panels show (a) BASE scenario O₃ concentrations, (b) GEOS-CHEM minus
 392 BASE , (c) H-CMAQ minus BASE, and (d), CESM2.2 minus BASE. Values are plotted clockwise,
 393 starting from the southwest corner of the CMAQ simulation domain, with the model's sigma coordinates.
 394
 395 **Table 1.** Statistical results of average O₃ concentrations (ppbv) at various vertical heights among the
 396 four boundaries for four CBC scenarios.

Vertical altitude	Boundary	BASE	H-CMAQ	GEOS-Chem	CESM2.2
0-3 km	South	31.7	27.3	25	26
	East	31.7	24.9	23.8	25.1
	North	31.7	39.5	36.4	47.4
	West	31.7	43.5	45.8	51.7
3-10 km	South	53.2	40.1	26.7	35.6
	East	53.2	54.9	43.4	61.7
	North	53.2	79.2	68.4	119.7
	West	53.2	76.2	60.6	88.7
Above 10 km	South	408.0	233.4	42.4	272.0
	East	408.0	351.6	82.0	373.8
	North	408.0	658.3	186.9	728.7
	West	408.0	338.6	88.2	324.1

397 **3.2 Evaluation of Model Performance Using Different CBC**

398 **3.2.1 Meteorological simulation evaluation**

399 Table 2 presents an evaluation of WRF model simulations of 2-meter temperature (T2),
 400 2-meter daily maximum temperature (T2max), 2-meter relative humidity (RH2), 10-
 401 meter wind speed (WS10), surface pressure (PRS), and precipitation (PRECIP). The
 402 data were averages from 2439 meteorological stations across China. Analysis of mean
 403 bias (MB), correlation coefficient (r), and index of agreement (IOA) reveals that the
 404 WRF model accurately simulated the meteorological fields. T2, T2max, RH2, and PRS
 405 exhibit IOA values exceeding 0.85, indicating strong agreement with observations.
 406 Correlation coefficients (r) exceed 0.7 for all variables except WS10. However, some
 407 biases remain in the simulation results for certain variables. Specifically, RH2 and PRS
 408 are slightly underestimated, while PRECIP is overestimated; nevertheless, the r and
 409 IOA values remain relatively high. In contrast, WS10 is significantly overestimated (by
 410 1.6 m/s), with both IOA and r below 0.5. This likely stems from the relatively coarse
 411 model grid resolution, hindering accurate representation of urban topography and its
 412 impact on wind speed—a phenomenon observed in other studies (Hu et al., 2016; Shen
 413 et al., 2022). Overall, the WRF model demonstrates good performance in
 414 meteorological simulations, providing reliable inputs for the CMAQ model.

415
 416

Table 2. Evaluation results for the meteorological variables.

variable	OBS	SIM	MB	RMSE	IOA	r
T2 (°C)	25	24.4	-0.6	2.1	0.94	0.91
T2max (°C)	29.9	29.3	-0.6	2.5	0.91	0.86
RH2 (%)	73.6	69.1	-4.5	8.6	0.88	0.86
WS10 (m/s)	2	3.6	1.6	1.8	0.41	0.45
PRS (hPa)	937.8	922.7	-15.1	28.5	0.97	0.97
PRECIP (mm)	297.4	434.3	136.9	234.2	0.72	0.7

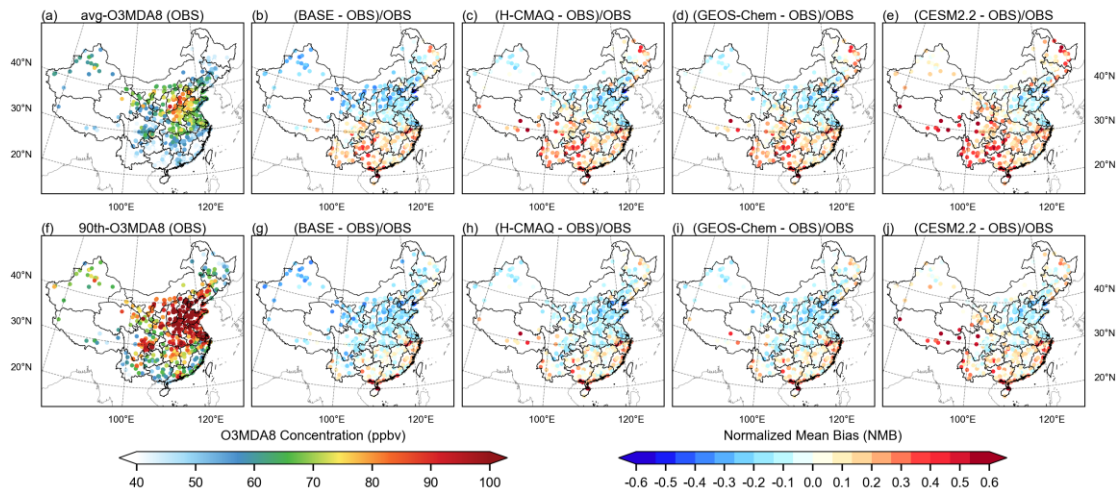
418 3.2.2 Surface O₃ Simulation Performance

419 Figure 3 illustrates the spatial distribution of avg-O₃MDA8 and 90th-O₃MDA8
 420 concentrations and their normalized mean bias (NMB) across China. Across all
 421 monitoring sites, the observed avg-O₃MDA8 and 90th-O₃MDA8 for July-August 2019
 422 are 59.4 ppbv and 82.8 ppbv, respectively (Table S3). Generally, O₃ concentrations in
 423 North China are higher than in South China. For 90th-O₃MDA8, elevated values are
 424 widespread, notably in the North China Plain (NCP), Central China, Yangtze River
 425 Delta (YRD), Pearl River Delta (PRD), and Sichuan Basin (SCB), highlighting the
 426 severity of summer O₃ pollution across China.

427 Substantial discrepancies exist between observed and simulated O₃ across all CBC
 428 scenarios. The BASE scenario, in particular, systematically underestimates both mean
 429 and extreme O₃, especially in northern regions (latitude > 30° N). Avg-O₃MDA8
 430 underestimations reach -16.1 ppbv in North China and -11.2 ppbv in Northwest China,
 431 with moderate underestimations in East (-5.1 ppbv) and Northeast China (-4.8 ppbv)
 432 (Fig. 3; Table S4). Similarly, 90th-O₃MDA8 was underestimated by 32.9% in North
 433 China and 26.2% in Northwest China, with smaller NMB (-9.3 to -14.2%) elsewhere
 434 except South China (Table S5). These results indicate that the BASE scenario poorly
 435 represents both average and high O₃ levels, limiting its ability to capture O₃ formation
 436 and transport processes during hot seasons.

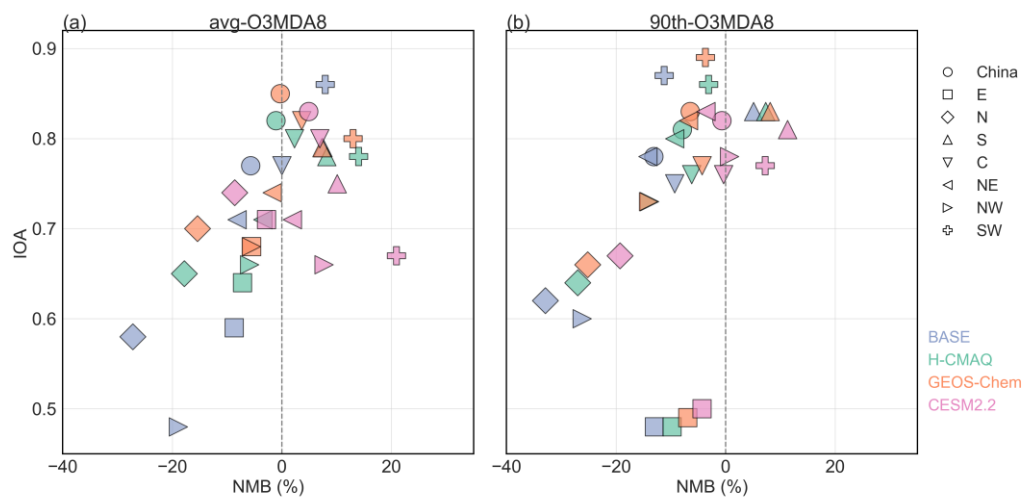
437 By incorporating global model-derived CBC, significant improvements in both bias and
 438 agreement are observed across China. Based on the NMB values for avg-O₃MDA8 and
 439 90th-O₃MDA8 of all sites, the three dynamic CBC scenarios performance can be
 440 ranked as follows: GEOS-Chem (-0.3%) > H-CMAQ (-1.1%) > CESM2.2 (+4.9%) for
 441 avg-O₃MDA8 and CESM2.2 (-0.7%) > GEOS-Chem (-6.5%) > H-CMAQ (-7.9%)
 442 for 90th-O₃MDA8 (Tables S4-S5). GEOS-Chem consistently yields the smallest bias in
 443 avg-O₃MDA8, indicating the most accurate representation of boundary and background
 444 O₃ inflow under average conditions. Notably, its normalized mean bias (NMB) falls
 445 within ±10% in five of the seven subregions—specifically, all except North and
 446 Northwest China—demonstrating that the GEOS-Chem scenario best captures overall
 447 ozone levels across China. Correspondingly, its index of agreement (IOA) reaches 0.85
 448 for avg-O₃MDA8 and 0.83 for 90th-O₃MDA8, the highest among all scenarios,
 449 suggesting excellent spatial and temporal consistency with observations. The H-CMAQ
 450 scenario also improves upon the BASE case, albeit to a slightly lesser extent, reducing
 451 O₃ underestimation while maintaining IOAs of 0.82 (avg-O₃MDA8) and 0.81 (90th-
 452 O₃MDA8). In contrast, the CESM2.2 scenario exhibits a positive NMB for avg-

453 O3MDA8 (+4.9%), suggesting a slight overestimation in background inflow. However,
 454 CESM2.2 substantially improved the simulation of O₃ extremes, with a much smaller
 455 NMB for all sites(-0.7%)for 90th-O3MDA8. The underestimation of high ozone
 456 concentrations and pollution episodes is significantly alleviated in five subregions:
 457 North, Northeast, Northwest, East, and Southwest China. This improvement is further
 458 underscored by a consistently high IOA of 0.83, highlighting CESM2.2's capability in
 459 accurately reproducing high-O₃ pollution events—particularly in regions characterized
 460 by complex terrain and intense photochemical activity. Overall, these results
 461 demonstrate that applying dynamic CBC derived from global chemical transport
 462 models substantially enhances the simulation of both average and extreme O₃
 463 concentrations. The CESM2.2 CBC may perform relatively better in simulating high
 464 ozone concentrations and pollution episodes.



465

466 **Figure 3.** Spatial distribution of avg-O3MDA8 and 90th-O3MDA8 from observations (OBS) and four
 467 CBC scenario simulations. Panels (a, f) show observed avg-O3MDA8 and 90th-O3MDA8 at 1480
 468 monitoring sites during July -August 2019, while panels (b-e, g-j) present site-level normalized mean
 469 bias (NMB) for BASE, H-CMAQ, GEOS-Chem, and CESM2.2 simulations, respectively.



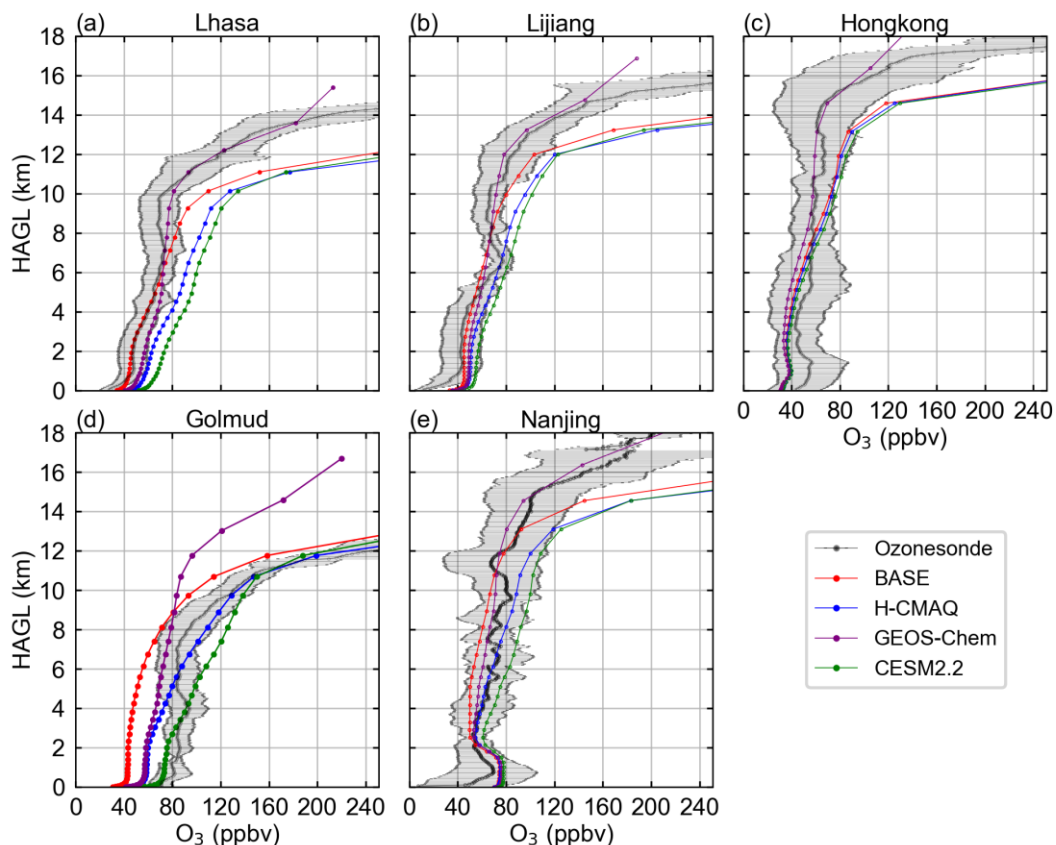
470

471 **Figure 4.** Comparison of model performance among four CBC scenarios (BASE, H-CMAQ, GEOS-
 472 Chem, and CESM2.2) in terms of Normalized Mean Bias (NMB, %) and Index of Agreement (IOA) for
 473 (a) average daily maximum 8-hour O₃ concentrations (avg-O3MDA8) and (b) the 90th percentile of daily

474 maximum 8-hour O₃ (90th-O₃MDA8) in China and its seven subregions (South (S), East (E), North (N),
 475 Central (C), Northeast (NE), Northwest (NW), and Southwest (SW)). Statistics are based on daily data
 476 from July–August 2019; number of monitoring sites: China (1480), E (319), N (181), S (256), C (204),
 477 NE (166), NW (154), and SW (200).

478 At the regional scale, however, differences among the three dynamic CBC scenarios
 479 become regionally differentiated (Fig. 4). Although GEOS-Chem and H-CMAQ
 480 consistently show the best nationwide performance, CESM2.2 demonstrates superior
 481 accuracy in several regions. For instance, CESM2.2 achieves the smallest NMB and
 482 highest IOA in the north (N), northeast (NE), east (E) and northwest (NW) regions for
 483 both avg-O₃MDA8 and 90th-O₃MDA8, reflecting its strength in capturing high O₃
 484 events in those areas. In the SW region, CESM2.2 outperforms other models with a
 485 positive NMB yet high IOA, indicating a well-aligned simulation of elevated
 486 background O₃ levels. In contrast, GEOS-Chem exhibits balanced performance across
 487 most regions, notably achieving relatively low NMB and high IOA in the east (E),
 488 central (C), and northeastern (NE) regions. These areas are typically influenced by
 489 continental outflow and moderate photochemistry, conditions under which GEOS-
 490 Chem’s background O₃ input appears to be well-optimized. H-CMAQ offers moderate
 491 improvement relative to the BASE scenario across most regions, with less extreme
 492 biases than BASE and slightly lower IOA compared to CESM2.2 or GEOS-Chem.

493 3.2.3 Vertical O₃ profile Evaluation



494
 495 **Figure 5.** Comparison of vertical O₃ profiles between four CBC scenario simulation (BASE, H-CMAQ,
 496 GEOS-Chem, and CESM2.2) and sounding observations at five stations across China. All profiles are

497 plotted against Height Above Ground Level (HAGL); statistics are based on vertical profile data
 498 summarized in Table S2 (including observation periods and site-specific information).

499
 500
 501

Table 3 Comparison and evaluation of vertical O₃ concentration profiles (ppbv) at each sounding station.

	Lhasa	Lijiang	Hongkong	Golmud	Nanjing
Lower troposphere (0-3 km)					
OBS	45.4	39.1	49.9	64.9	57.9
BASE	45.3	45.1	40.8	43.0	64.8
H-CMAQ	60.6	50.6	41.3	59.4	67.0
GEOS-Chem	54.8	48.8	39.5	57.5	67.3
CESM2.2	70.4	55.7	41.9	74.6	71.0
Mid-to-upper troposphere (3-10 km)					
OBS	66.7	62.1	53.9	85.0	68.2
BASE	75.1	62.0	51.4	62.7	56.1
H-CMAQ	94.9	74.8	53.9	94.7	71.5
GEOS-Chem	72.6	62.9	45.8	73.8	62.2
CESM2.2	104.0	81.4	56.7	112.0	83.5
lower stratosphere (10-16 km)					
OBS	230.8	122.1	68.1	174.6	92.3
BASE	306.6	211.7	106.5	288.1	117.7
H-CMAQ	394.4	259.3	112.8	367.7	149.7
GEOS-Chem	147.5	106.6	66.8	131.8	85.7
CESM2.2	371.3	249.3	116.0	332.6	153.8

502 To assess the performance of the model in simulating vertical O₃ distribution under
 503 different CBC, we compare the simulated O₃ profiles from the four scenarios with
 504 observational data from five ozonesonde stations (Fig. 5). To better evaluate model
 505 performance at different altitudes, we compute mean O₃ concentrations within three
 506 representative vertical layers: the lower troposphere (0–3 km), the middle-to-upper
 507 troposphere (3–10 km), and the lower stratosphere (10–16 km), as summarized in Table
 508 3.

509 In lower troposphere (0–3km), observed O₃ concentrations in this layer ranged from
 510 ~39 to 65 ppbv across the five sites. O₃ concentrations in the lower troposphere are
 511 sensitive to both local emissions and background inflow. The BASE scenario generally
 512 underestimates O₃, whereas incorporating dynamic CBC increased near-surface
 513 concentrations. Among the scenarios, GEOS-Chem exhibits the most balanced
 514 performance, with mean biases typically within ± 10 ppbv. CESM2.2 overestimates O₃
 515 substantially at high-altitude sites, e.g., +25.0 ppbv at Lhasa and +9.7 ppbv at Golmud,
 516 indicating excessive inflow of near-surface O₃. H-CMAQ also slightly overestimates
 517 O₃, but with smaller magnitudes. These results indicate that while dynamic CBC
 518 improve near-surface O₃ representation, overestimation in clean or elevated regions
 519 (e.g., Lhasa) must be carefully considered, especially when using CESM2.2.

520 The mid-to-upper troposphere (3~10km) reflects regional background transport, deep
521 convection, and vertical mixing. Observed O₃ levels typically increase with altitude,
522 ranging from ~54 to 85 ppbv. The BASE scenario consistently underestimates O₃ in
523 this layer, particularly in Golmud (-22.3 ppbv) and Nanjing (-12.1 ppbv), due to
524 insufficient O₃ inflow. Dynamic CBC significantly reduces this bias. H-CMAQ and
525 CESM2.2 both improve model-observation agreement, but CESM2.2 often
526 overestimates O₃ (e.g., +37.3 ppbv in Lhasa), potentially reflecting overly strong
527 entrainment of free-tropospheric O₃. GEOS-Chem again performs best overall,
528 producing values close to observations in Lijiang, Nanjing, and Lhasa, demonstrating
529 a good balance between under- and overestimation. This suggests that GEOS-Chem
530 CBC offer the most realistic representation of free-tropospheric O₃, while CESM2.2
531 may be too aggressive in polluted or convective regions.

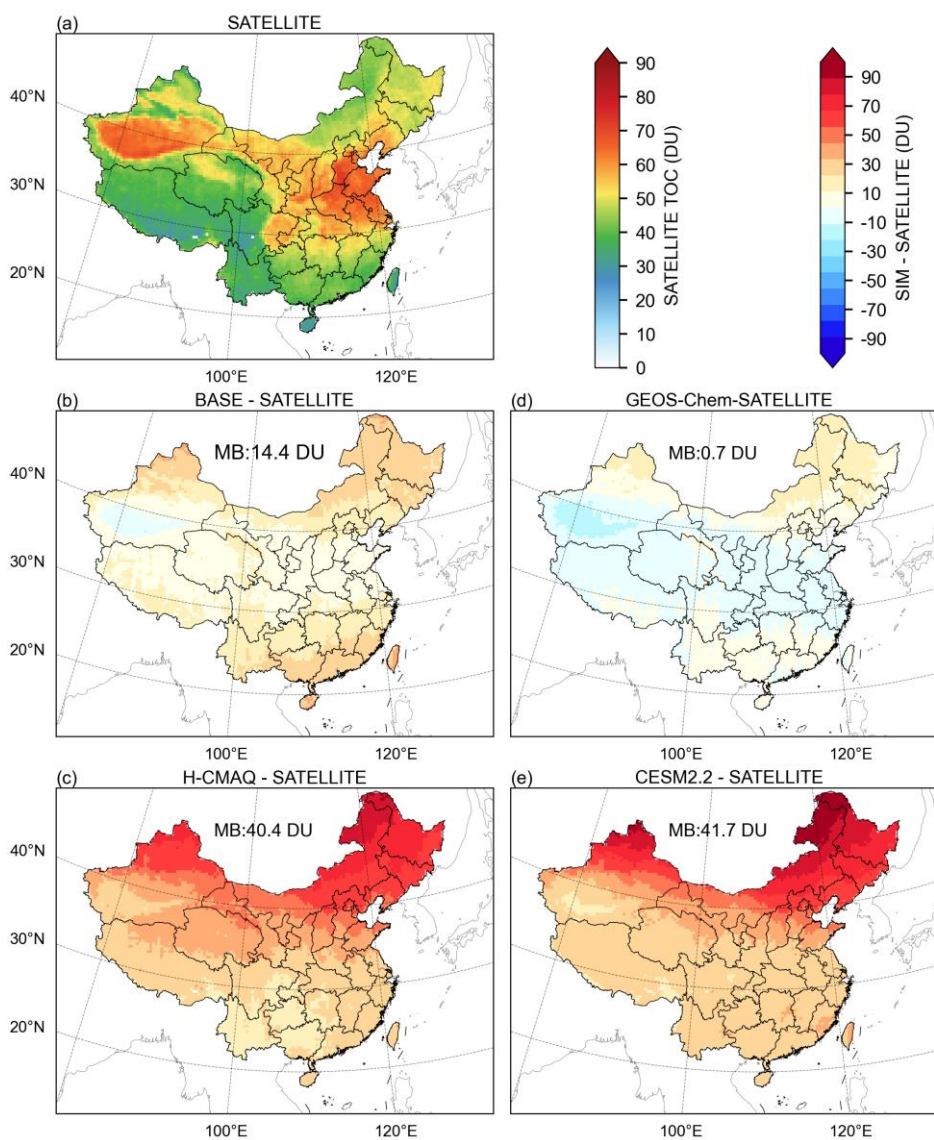
532 In the lower stratosphere (10–16 km), O₃ levels increase sharply in this layer, with
533 observed values ranging from ~68 to 231 ppbv. The BASE scenario significantly
534 overestimates stratospheric O₃ at all sites, especially in Golmud and Lhasa, indicating
535 excessive intrusion of stratospheric O₃ in default boundary inputs. This bias is further
536 amplified in H-CMAQ and CESM2.2, with overestimations exceeding ~164 ppbv and
537 ~140 ppbv in Lhasa and ~193 ppbv and ~158 ppbv in Golmud. From the vertical O₃
538 profile comparison, the elevated biases in the lower stratosphere of BASE, H-CMAQ,
539 and CESM2.2 scenarios may enhance the stratosphere-troposphere exchange (STE),
540 especially in southwestern and southern China, which is significantly influenced by the
541 Qinghai-Tibet Plateau (Fig. 5a-c,e). In contrast, GEOS-Chem was the only CBC that
542 consistently reduced this overestimation, bringing modeled values closer to
543 observations at all sites. For example, it lowers the stratospheric bias in Golmud from
544 +113.5 ppbv (BASE) to -42.8 ppbv and achieved near-perfect agreement in Hong Kong
545 (-1.3 ppbv). Overall, the vertical profile analysis underscores that GEOS-Chem
546 provides the most accurate representation of upper tropospheric and stratospheric O₃
547 inflow, especially important for western China where STE processes are more active.

548 **3.2.4 Satellite-Based O₃ Column Assessment**

549 The spatial distribution of tropospheric ozone column (TOC) concentrations provides
550 valuable insights into regional O₃ pollution patterns. In this study, TOC concentrations
551 retrieved from the Environmental Trace Gases Monitoring Instrument (EMI) aboard the
552 Gaofen-5 satellite during July–August 2019 were compared with simulation (SIM)
553 results from four different scenario models (Fig. 6). Observational data from EMI
554 indicate a general increase in TOC concentrations with latitude across China, consistent
555 with previous studies (Zhu et al., 2022; Liu et al., 2022). North China exhibits the
556 highest TOC values among the eastern regions, corresponding to areas known for severe
557 surface-level O₃ pollution (Lu et al., 2018).

558 From the numerical modeling perspective, the simulation scenarios based on the BASE,
559 H-CMAQ, and CESM2.2 models predominantly reflect an overestimation of TOC
560 concentrations. Among them, the BASE scenario demonstrates the least degree of
561 overestimation, particularly in the South China and Northeast China regions, where
562 overestimations range from 20 to 30 DU, while other regions exhibit overestimations
563 between 10 and 20 DU. Both the H-CMAQ and CESM2.2 models show robust

564 overestimations exceeding 20 DU, especially in northern China (north of 35°N), where
 565 the overestimation can surpass 40 DU, with the Northeast region registering the highest
 566 overestimation, reaching beyond ~50—60 DU. In contrast, the CBC boundary
 567 conditions provided by the GEOS-Chem model yield superior results in simulating the
 568 spatial distribution of TOC, with slight overestimations noted in South China and areas
 569 north of 40°N, while underestimating concentrations within the latitude range of 30°N
 570 to 40°N. The regional mean bias (MB) of model-simulated TOC versus satellite
 571 observations was calculated for the mainland of China. The MB of model-simulated
 572 TOC (DU) for the four scenarios—BASE, H-CMAQ, CESM2.2, and GEOS-Chem—
 573 is 14.4 DU, 40.4 DU, 41.7 DU, and 0.7 DU, respectively, consistent with the analysis
 574 results shown in Fig. 5. And the simulation discrepancies for TOC across China are
 575 confined to approximately ± 10 DU, indicating that GEOS-Chem's CBC represent the
 576 optimal boundary condition input for regional O₃ modeling in China area.



577

578 **Figure 6.** Comparison of tropospheric ozone column (TOC) distributions over China between satellite
 579 observations and model simulations. Panel (a) shows the TOC retrieved from satellite measurements,
 580 while panels (b–e) depict the differences (MB) between simulated TOC from the BASE, H-CMAQ,

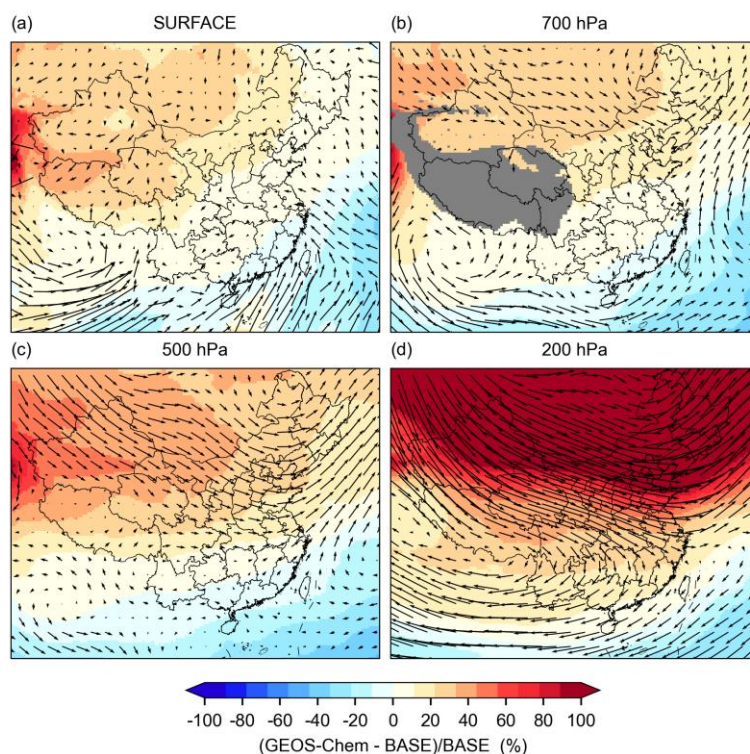
581 GEOS-Chem, and CESM2.2 scenarios and the satellite retrieval.

582

583 3.3 Mechanism of the impact of CBC on O₃ formation

584 3.3.1 General impact of synoptic-scale circulation

585 CBC regulate regional O₃ by controlling the inflow of background O₃ and precursors at
586 model boundaries. Given the superior performance of GEOS-Chem in reproducing
587 surface and vertical O₃ based on our validations, we further contrast GEOS-Chem with
588 the BASE scenario to highlight the role of CBC in cross-boundary transport at the
589 surface and at 700, 500, and 200 hPa isobaric surfaces (Fig. 7).



590

591 **Figure 7.** Normalized mean bias (NMB, (GEOS-Chem – BASE)/BASE) of mean O₃ concentrations and
592 corresponding mean flow fields at surface and 700, 500, and 200 hPa isobaric surfaces over the
593 simulation domain. (The grey area indicates invalid value.)

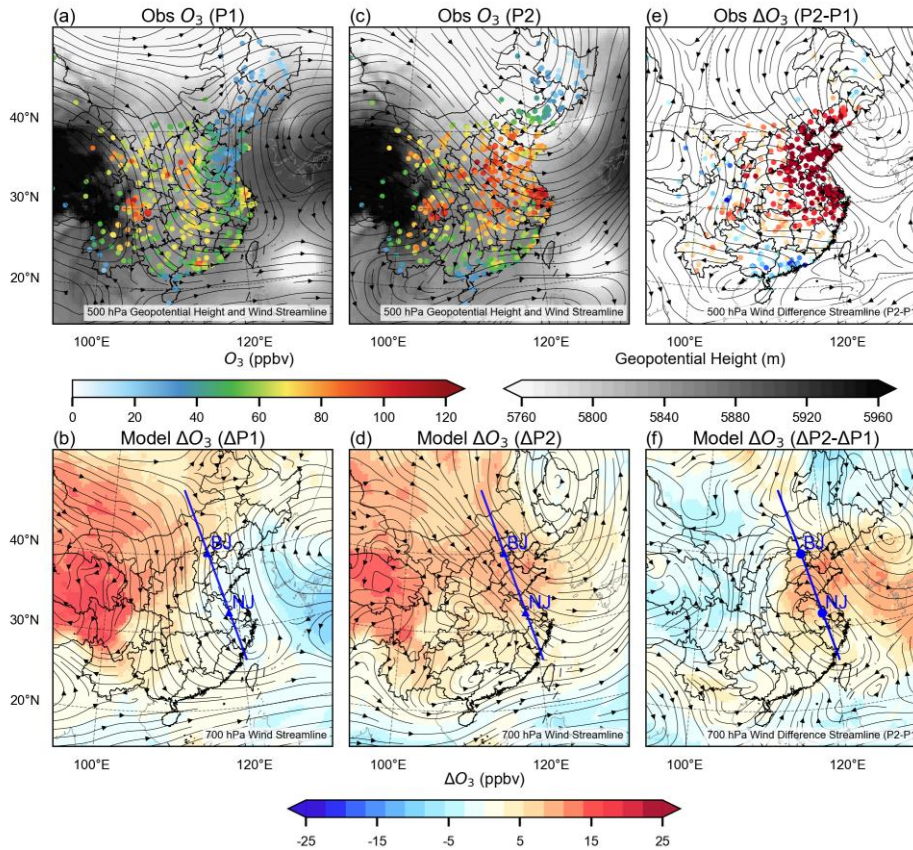
594 In southeastern China, summer monsoonal flow carries relatively clean marine air into
595 the mid–lower troposphere, lowering background O₃ and suppressing accumulation
596 over eastern and southern regions, where GEOS-Chem boundary conditions produce
597 slightly reduced concentrations (<4%, Fig. 7a-7b). This dilution effect is consistent with
598 the characteristic influence of the Western Pacific Subtropical High during summer,
599 which effectively flushes the coastal boundary layer with cleaner oceanic air masses. In
600 contrast, along the northern and western boundaries, GEOS-Chem introduces
601 substantially higher O₃ than BASE. Advected by prevailing northwesterlies, these
602 inflows penetrate deep into inland China, increasing surface O₃ by more than 10%
603 across most regions and by over 20% in northern and northwestern China. The
604 magnitude of this enhancement aligns with the recognized impact of long-range
605 transport from Eurasia, which often elevates the ozone baseline in northern China. The
606 influence of CBC is even stronger at higher altitudes (Fig. 7c-7d). At 500 and 200 hPa,
607 GEOS-Chem introduces markedly higher O₃ than BASE, reflecting enhanced

608 background inflows and contributions from stratospheric air masses. This vertical
609 gradient in CBC sensitivity underscores the role of the free troposphere as a reservoir
610 for long-lived O₃. Such upper-level enhancements have important surface implications,
611 as downward mixing and stratosphere–troposphere exchange (STE) can transport high-
612 O₃ air into the boundary layer under favorable meteorological conditions, especially
613 during the passage of cold fronts or deep convective mixing, further exacerbating
614 pollution episodes.

615 Overall, these results highlight that the mechanistic impact of CBC on O₃ formation
616 arises from a synergistic combination of boundary inflow composition and large-scale
617 circulation. While oceanic inflows tend to dilute O₃ in southern and eastern regions,
618 strong continental and stratospheric inflows from the north and west can significantly
619 elevate both free-tropospheric and surface O₃, amplifying pollution severity in inland
620 China. These findings confirm that accurate CBC are not merely a model constraint but
621 a vital component for capturing the dynamic interplay between local photochemistry
622 and global atmospheric circulation.

623 **3.3.2 Case Study: Synoptic-Scale Circulation Dynamics Modulating CBC** 624 **Impacts**

625 The influence of CBC varies dynamically with large-scale meteorological conditions
626 rather than remaining static. During summer, synoptic disturbances such as the Western
627 Pacific Subtropical High extensions, tropical cyclone activity, and East Asian westerly
628 jet fluctuations reshape regional circulation patterns and modulate the transport of
629 polluted or clean air masses into the model domain. These circulation changes,
630 characterized by alternating cyclonic and anticyclonic flows, substantially alter the
631 efficiency of transboundary transport and consequently affect CBC impacts on near-
632 surface O₃ simulations. Here, we examine two sequential circulation regimes during
633 August 2019 associated with successive typhoon events: Super Typhoon Lekima and
634 Typhoon Krosa. These events create distinctly different transport patterns that
635 modulated how boundary conditions influenced surface O₃ across China. Based on this
636 evolution, we define two phases: Phase 1 (P1, 10–14 August, during Lekima's landfall
637 and decay in Eastern China) and Phase 2 (P2, 15–19 August, controlled by post-trough
638 northwesterlies) (Fig. 8).



639

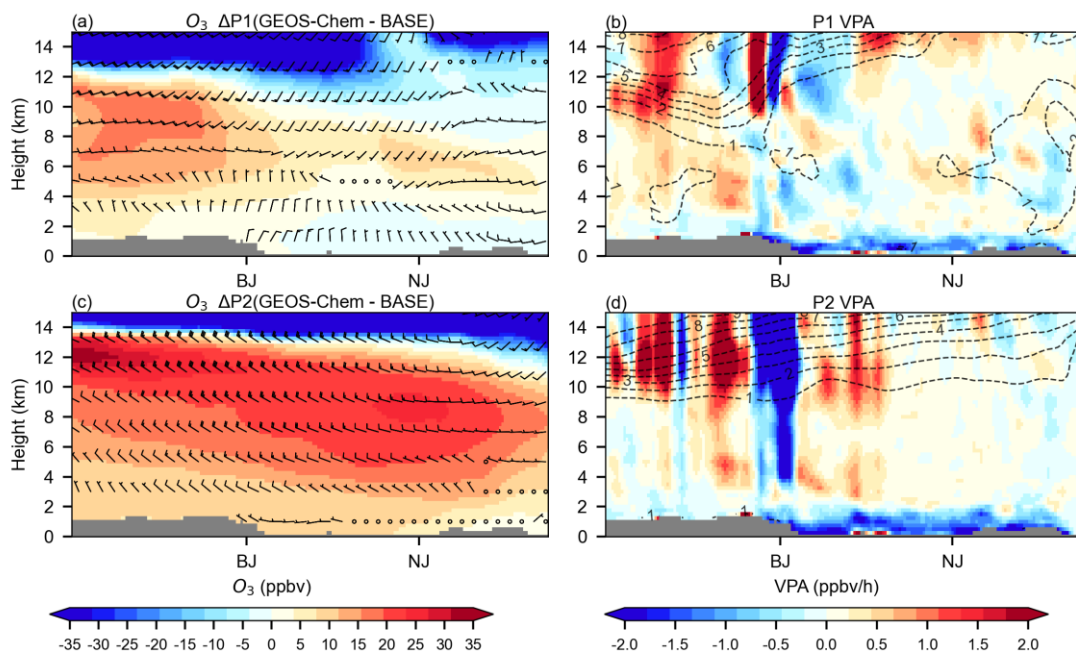
640 **Figure 8.** (a) Distribution of 500 hPa winds (streamlines), geopotential height (contours), and surface O_3
 641 observations (dots) during P1; (b) Distribution of 700 hPa winds (streamlines), and difference in modeled
 642 surface O_3 between GEOS-Chem CBC and BASE during P1; (c) same as (a) but for P2; (d) same as (b)
 643 but for P2; (e) differences in observed surface O_3 and 500 hPa winds between P1 and P2; (f) differences
 644 in simulated surface O_3 and 700 hPa winds between P1 and P2. Blue lines indicate the locations of vertical
 645 cross-sectional analyses, extending from north to south through Beijing (BJ) and Nanjing (NJ).

646 P1 occurs during the landfall and decay of Super Typhoon Lekima over the Yangtze
 647 River Delta (Fig 8a and 8b, and Fig. S2). The tropospheric circulation is dominated by
 648 a deep trough linked to the typhoon's remnant system, which enhances southeasterly
 649 flow of marine air into eastern China. This pattern promotes deep convection and
 650 vigorous vertical mixing, leading to a pronounced coastal-inland gradient in surface O_3 :
 651 marine-influenced coastal areas exhibit low concentrations (<50 ppbv), while inland
 652 regions maintain moderate-to-high levels (60–90 ppbv). The cyclonic circulation
 653 disrupts typical westerly transport pathways, reducing transboundary O_3 influence from
 654 northern and western source regions. Consequently, the BASE scenario overestimates
 655 O_3 by 15-25 ppbv over oceanic regions where static boundary conditions fail to capture
 656 typhoon-enhanced marine influence, while underestimating concentrations by 10-20
 657 ppbv in northwestern China where continental transport remains active but was
 658 inadequately represented by the Pacific-based boundary profile (Fig. 8b).

659 By contrast, P2 is characterized by a dominant northwesterly flow across central and
 660 eastern China, situated behind a mid-level trough, while a high-pressure system
 661 strengthened over western China (Fig. 8c-8d). This "east-trough, west-ridge"
 662 configuration facilitates the efficient advection of O_3 -rich air from western and northern
 663 source regions, resulting in the noticeable O_3 elevations observed across the region (Fig.

664 8c-d). Model sensitivity analysis confirms that accurately representing these high-O₃
 665 boundary inflows under such transport-favorable conditions elevates surface
 666 concentrations by 10–15 ppbv in the most affected areas (Fig. 8d). These results
 667 demonstrate that the BASE scenario, employing static boundary conditions,
 668 systematically underestimates cross-boundary pollution contributions during
 669 dynamically active periods when long-range transport is of importance.
 670 The difference between P2 and P1 (Fig. 8e–f) illustrates a marked meteorological
 671 transition from a pollution-scavenging cyclonic regime during P1 to a pollution-
 672 accumulating regime in P2, characterized by trough-driven northwesterly transport and
 673 high-pressure-induced stability. This synoptic shift corresponds with observed surface
 674 O₃ increases of 30–60 ppbv across northern and central-eastern China. These regions
 675 align spatially with the anticyclonic circulation, where enhanced subsidence favors the
 676 accumulation of transported O₃. By incorporating chemically realistic CBC, the
 677 simulation attributes approximately 10 ppbv of this O₃ increase to cross-boundary
 678 transport during P2 (Fig. 8f), highlighting the essential role of CBC in accurately
 679 capturing O₃ buildup under transport-favorable synoptic regimes.

680



681

682 **Figure 9.** (a) Vertical cross-sectional analysis of the O₃ difference between GEOS-Chem CBC and the
 683 BASE scenario during P1, the wind bar denotes vertical wind field; (b) vertical distribution of potential
 684 vorticity (PV, dashed contours) and vertical transport (VPA, calculated by CMAQ process analysis as the
 685 sum of vertical diffusion and vertical advection) during P1; (c) same as (a) but for P2. (d) same as (b) but
 686 for P2. The x-axis labels BJ and NJ indicate the locations of Beijing and Nanjing, respectively.

687 To further clarify the role of dynamic CBC in O₃ simulations, we perform vertical cross-
 688 sectional analyses using the CMAQ process analysis module along the major transport
 689 pathways during P1 and P2 (Fig. 9). Both phases consistently reveal strong cross-
 690 boundary transport, with upstream inflows from outside the domain substantially
 691 influencing downstream O₃ levels across mainland China. During P1, Typhoon Lekima
 692 disrupts the transport corridor near the Yangtze River Delta (approximately 0–4 km),

693 restricting cross-boundary influences mainly to northern inflows affecting the North
694 China Plain (Fig. 9a). In contrast, under post-trough northwesterly flow during P2,
695 cross-boundary transport extends southward from the northern boundary, reaching as
696 far as the Yangtze River Delta (Fig. 9b). The difference between P1 and P2 highlights
697 a distinct transport corridor extending from higher to lower latitudes and from the mid-
698 upper troposphere toward the surface (Fig. S3), further emphasizing the crucial role of
699 dynamic CBC in shaping O₃ distributions.

700 Here, we demonstrate that cross-boundary transport also occurs in the vertical
701 dimension, with O₃-rich air descending from the upper to the lower troposphere, while
702 stratosphere-troposphere exchange (STE) provides an additional pathway for
703 transboundary inflow. To identify possible STE occurrences, potential vorticity (PV)
704 between 10 and 14 km (above sea level) is examined, adopting a threshold of 2 PVU
705 (PV units, 1 PVU = 10⁻⁶ m⁻² s⁻¹ kg⁻²) to distinguish stratospheric from tropospheric air
706 masses. STE events are evident over northern China during both P1 and P2 (Fig. 9c-d
707 and Fig. S4). In addition, the CMAQ process analyses with GEOS-Chem CBC
708 corroborate intensified vertical transport between 10 and 14 km in both phases, with
709 distinctly positive contributions from vertical advection and turbulent diffusion. As a
710 result, the joint impact of large-scale advection and vertical mixing processes enables
711 high-altitude O₃ to intrude into the lower troposphere and ultimately affect downstream
712 regions, even in YRD (such as Nanjing city).

713 **4. Conclusion**

714 This research demonstrates that CBC represent a critical but often underappreciated
715 component of regional air quality modeling systems. We systematically evaluated the
716 influence of CBC on regional O₃ simulations over China using the WRF-CMAQ model.
717 Four CBC scenarios were compared: a static BASE scenario using climatological
718 profiles and three dynamic scenarios derived from global chemical transport models
719 (H-CMAQ, GEOS-Chem, and CESM2.2). Overall, dynamic CBC substantially
720 improve the representation of surface O₃ compared to the static BASE scenario, with
721 GEOS-Chem CBC performing the best. Across China, the normalized mean bias (NMB)
722 for avg-O3MDA8 is reduced from -5.7% (BASE) to -0.3% (GEOS-Chem), and the IOA
723 increased from 0.77 to 0.85, while the 90th-O3MDA8 percentile NMB improved from
724 -13.1% to -6.5%, and the IOA increased from 0.66 to 0.77. Based on ozonesonde
725 profiles and satellite TOC evaluations, elevated biases are identified in the lower
726 stratosphere for BASE, H-CMAQ, and CESM2.2, which may lead to overestimation of
727 background O₃ concentrations, particularly during STE events.

728 The influence of CBC varies dynamically with large-scale meteorological conditions
729 rather than remaining static. During summer, synoptic disturbances such as the Western
730 Pacific Subtropical High extensions, tropical cyclone activity, and East Asian westerly
731 jet fluctuations reshape regional circulation patterns and modulate the transport of
732 polluted or clean air masses into the model domain. These circulation changes,
733 characterized by alternating cyclonic and anticyclonic flows, substantially alter the
734 efficiency of transboundary transport and consequently affect CBC impacts on near-

735 surface O₃ simulations. Generally, oceanic inflows from the south dilute O₃ in
736 southeastern and coastal areas, whereas strong continental and stratospheric inflows
737 from northern and western boundaries significantly modulate tropospheric O₃,
738 especially in downwind regions of the synoptic systems.

739 A comparative analysis of two successive synoptic regimes in July - August 2019,
740 which shifted from a cyclone-dominated, pollution-scavenging phase to a post-trough
741 northwesterly flow favorable for accumulation, reveals that dynamic circulation
742 patterns enhance cross-boundary transport both horizontally (via continental inflows
743 from northern and western boundaries) and vertically (via stratosphere-troposphere
744 exchange). The combined effects of these transport processes increase O₃
745 concentrations by 10–20% during high-pollution events over eastern China. These
746 results underscore that accurate representation of dynamic CBC is essential to capture
747 circulation-driven horizontal and vertical transport and their integrated impact on
748 regional O₃ distributions. Regarding the representativeness of these findings, while this
749 study focuses on summer 2019, the selected period captures representative
750 meteorological regimes of the East Asian summer monsoon, including typical
751 southeasterly marine flows and northwesterly continental inflows. The inclusion of
752 typhoon-induced circulation changes (e.g., Lekima and Krosa) further ensures that the
753 findings reflect common synoptic disturbances affecting regional air quality. Although
754 quantitative magnitudes may vary with interannual climate variability, the identified
755 mechanisms regarding CBC sensitivity under transport-favorable conditions are
756 applicable to typical summer pollution episodes in monsoon-affected regions.

757 Our findings demonstrate that the choice of CBC is not merely a technicality but a
758 dynamic determinant of simulated O₃ levels for regional CTM, especially when facing
759 synoptic regimes that favor long-range transport or vertical exchange. This underscores
760 the necessity of moving beyond static boundary conditions in regional air quality
761 modeling. Static CBC remain a common baseline in regional modeling, with recent
762 assessments indicating that a majority of studies still rely on default or unspecified
763 boundary conditions (Zhu et al., 2024). While the simplified BASE scenario may not
764 represent the most realistic boundary condition, it serves as a controlled baseline to
765 isolate the incremental value of time-varying CBC, which is the primary focus of this
766 study. To advance predictive capability, future efforts should pursue multi-model
767 ensembles to quantify CBC uncertainty, evaluate 3-D climatological boundary
768 conditions as a refined benchmark and explore the integration of real-time global fields
769 into regional CTM forecasting systems. By elucidating the critical interplay between
770 large-scale transport and regional pollution, this study provides a scientific foundation
771 not only for improving O₃ forecasting but also for designing effective transboundary air
772 quality management strategies.

773 **Acknowledgments**

774 This research is supported by the National Key Research and Development Program
775 (grant no. 2023YFC3709301), the National Natural Science Foundation Project (grant
776 no. 42575120), the Youth Fund Project of the Sichuan Provincial Natural Science
777 Foundation (24NSFSC2988), the Fundamental Research Funds for the Central
778 Universities (Grant No. YJ202313). We acknowledge use of the hyperspectral remote
779 sensing products of atmospheric compositions developed by Prof. Cheng Liu's group
780 at the University of Science and Technology of China. Numerical computations were

781 performed on Hefei advanced computing center. We also thank the Tsinghua University
782 for developing and sharing the MEIC emission inventory.

783 **Financial Support**

784 This research is supported by the National Key Research and Development Program
785 (grant no. 2023YFC3709301), the National Natural Science Foundation Project (grant
786 no. 42575120), the Youth Fund Project of the Sichuan Provincial Natural Science
787 Foundation (24NSFSC2988), the Fundamental Research Funds for the Central
788 Universities (Grant No. YJ202313).

789 **Author Contributions**

790 N.W. and F.Y. designed the research. Y.D. conducted the simulation. Y.D. and N.W.
791 wrote the manuscript. S.L., Y.H., B.L. and G.S. contributed to the interpretation of the
792 results. R.H., B.L., Y.J., N.W. and Y.F. provided critical feedback and helped to improve
793 the manuscript.

794 **Competing Interests**

795 The authors declare that they have no known competing financial interests or personal
796 relationships that could have appeared to influence the work.

797 **Data Availability**

798 The observational datasets used in this study are publicly available from the following
799 sources: surface meteorological data from the China Meteorological Administration
800 (<http://data.cma.cn>, last access: 4 Apr. 2026); surface O₃ concentrations from the China
801 National Environmental Monitoring Center (<https://air.cnemc.cn:18007>, last access: 4
802 Apr. 2026); ozonesonde profiles from the World Ozone and Ultraviolet Radiation Data
803 Centre (WOUDC, <https://woudc.org>, last access: 4 Apr. 2026), the China Air Pollution
804 Data Center (CAPDC, <https://www.capdatabase.cn>, last access: 4 Apr. 2026), and the
805 National Tibetan Plateau Data Center (TPDC, <https://data.tpdc.ac.cn>, last access: 4 Apr.
806 2026); and tropospheric O₃ column data from the EMI/GF-5 product (Zhao et al., 2024).
807 Meteorological boundary conditions data derived from the ERA5 reanalysis dataset
808 (Hersbach et al., 2023) are available at <https://doi.org/10.24381/cds.adbb2d47>. The
809 MEIC v1.4 and MIX v1.1 emission inventories are available at <http://meicmodel.org>.
810 Global chemical model outputs used as boundary conditions are available from the
811 EQUATES project (H-CMAQ, <https://www.epa.gov/cmaq/EQUATES>, last access: 4
812 Apr. 2026), GEOS-Chem (<https://geoschem.github.io/>, last access: 4 Apr. 2026), and
813 CESM2.2/CAM-chem (<https://www2.acom.ucar.edu/gcm/cam-chem>, last access: 4
814 Apr. 2026). The WRF v3.9.1 (<https://github.com/wrf-model/WRF>, last access: 4 Apr.
815 2026) and CMAQ v5.3.3 (<https://github.com/USEPA/CMAQ>) model source codes are
816 open-source and publicly accessible via their official GitHub repositories. The custom
817 scripts developed for processing global model outputs into CMAQ-compatible
818 boundary conditions have been archived in the Zenodo repository under DOI:
819 [10.5281/zenodo.19447294]. Additional model results are stored on Shuguang high-
820 performance computing system and available from the corresponding author upon

821 reasonable request (nan.wang@scu.edu.cn).

822

823 **References**

824 Bai, L., Wang, J., Ma, X., and Lu, H.: Air pollution forecasts: An overview, *International journal of*
825 *environmental research and public health*, 15, 780, 2018.

826 Bai Zhixuan, B. J.: Golmud site SWOP atmospheric composition agent open line data (2020 -2021),
827 National Tibetan Plateau Data Center [dataset], 10.11888/Atmos.tpd.c.300057, 2022.

828 Bai Zhixuan, B. J.: Lijiang SWOP atmospheric composition comprehensive sounding data set
829 (2021-2022), National Tibetan Plateau Data Center [dataset], 10.11888/Atmos.tpd.c.300156, 2023.

830 Byun, D. and Schere, K. L.: Review of the governing equations, computational algorithms, and other
831 components of the Models-3 Community Multiscale Air Quality (CMAQ) modeling system,
832 *Applied mechanics reviews*, 59, 51-77, 2006.

833 Campbell, P. C., Bash, J. O., and Spero, T. L.: Updates to the Noah land surface model in WRF-
834 CMAQ to improve simulated meteorology, air quality, and deposition, *Journal of Advances in*
835 *Modeling Earth Systems*, 11, 231-256, 2019.

836 Carter, W. P. and Heo, G.: Development of revised SAPRC aromatics mechanisms, *Atmospheric*
837 *environment*, 77, 404-414, 2013.

838 Chiu, Y.-H. M., Wilson, A., Hsu, H.-H. L., Jamal, H., Mathews, N., Kloog, I., Schwartz, J., Bellinger, D.
839 C., Khani, N., and Wright, R. O.: Prenatal ambient air pollutant mixture exposure and
840 neurodevelopment in urban children in the Northeastern United States, *Environmental research*,
841 233, 116394, 2023.

842 Dou, X., Yu, S., Li, J., Sun, Y., Song, Z., Yao, N., and Li, P.: The WRF-CMAQ Simulation of a Complex
843 Pollution Episode with High-Level O₃ and PM_{2.5} over the North China Plain: Pollution
844 Characteristics and Causes, *Atmosphere*, 15, 198, 2024.

845 Eastham, S. D., Weisenstein, D. K., and Barrett, S. R.: Development and evaluation of the unified
846 tropospheric-stratospheric chemistry extension (UCX) for the global chemistry-transport model
847 GEOS-Chem, *Atmospheric Environment*, 89, 52-63, 2014.

848 Foley, K. M., Pouliot, G. A., Eyth, A., Aldridge, M. F., Allen, C., Appel, K. W., Bash, J. O., Beardsley, M.,
849 Beidler, J., and Choi, D.: 2002–2017 anthropogenic emissions data for air quality modeling over
850 the United States, *Data in Brief*, 47, 109022, 2023.

851 Gao, C., Zhang, X., Xiu, A., Tong, Q., Zhao, H., Zhang, S., Yang, G., Zhang, M., and Xie, S.:
852 Intercomparison of multiple two-way coupled meteorology and air quality models (WRF v4. 1.1–
853 CMAQ v5. 3.1, WRF-Chem v4. 1.1, and WRF v3. 7.1–CHIMERE v2020r1) in eastern China,
854 *geoscientific model development*, 17, 2471-2492, 2024.

855 Geng, G., Liu, Y., Liu, Y., Liu, S., Cheng, J., Yan, L., Wu, N., Hu, H., Tong, D., and Zheng, B.: Efficacy
856 of China's clean air actions to tackle PM_{2.5} pollution between 2013 and 2020, *Nature Geoscience*,
857 17, 987-994, 2024.

858 Godowitch, J. M., Gilliam, R. C., and Roselle, S. J.: Investigating the impact on modeled ozone
859 concentrations using meteorological fields from WRF with an updated four-dimensional data
860 assimilation approach, *Atmospheric Pollution Research*, 6, 305-311, 2015.

861 Goldberg, D. L., Vinciguerra, T. P., Hosley, K. M., Loughner, C. P., Canty, T. P., Salawitch, R. J., and
862 Dickerson, R. R.: Evidence for an increase in the ozone photochemical lifetime in the eastern United
863 States using a regional air quality model, *Journal of Geophysical Research: Atmospheres*, 120,

864 12778-12793, 2015.

865 Grell, G. A., Peckham, S. E., Schmitz, R., McKeen, S. A., Frost, G., Skamarock, W. C., and Eder, B.:
866 Fully coupled "online" chemistry within the WRF model, *Atmospheric environment*, 39, 6957-6975,
867 2005.

868 Hersbach, H., Bell, B., Berrisford, P., Biavati, G., Horányi, A., Muñoz Sabater, J., Nicolas, J., Peubey,
869 C., Radu, R., and Rozum, I.: ERA5 hourly data on pressure levels from 1940 to present, Copernicus
870 climate change service (c3s) climate data store (cds), 10, 24381, 2023.

871 Hogrefe, C., Liu, P., Pouliot, G., Mathur, R., Roselle, S., Flemming, J., Lin, M., and Park, R. J.: Impacts
872 of different characterizations of large-scale background on simulated regional-scale ozone over
873 the continental United States, *Atmospheric Chemistry and Physics*, 18, 3839-3864, 2018.

874 Hu, J., Chen, J., Ying, Q., and Zhang, H.: One-year simulation of ozone and particulate matter in
875 China using WRF/CMAQ modeling system, *Atmospheric Chemistry and Physics*, 16, 10333-10350,
876 2016.

877 Jacob, D. J.: The oxidizing power of the atmosphere, *Handbook of weather, climate and water*, 29-
878 46, 2003.

879 Jerrett, M., Arain, A., Kanaroglou, P., Beckerman, B., Potoglou, D., Sahsuvaroglu, T., Morrison, J.,
880 and Giovis, C.: A review and evaluation of intraurban air pollution exposure models, *Journal of*
881 *Exposure Science & Environmental Epidemiology*, 15, 185-204, 2005.

882 Lei, Y., Wu, K., Zhang, X., Kang, P., Du, Y., Yang, F., Fan, J., and Hou, J.: Role of meteorology-driven
883 regional transport on O₃ pollution over the Chengdu Plain, southwestern China, *Atmospheric*
884 *Research*, 285, 10.1016/j.atmosres.2023.106619, 2023.

885 Li, M., Liu, H., Geng, G., Hong, C., Liu, F., Song, Y., Tong, D., Zheng, B., Cui, H., and Man, H.:
886 Anthropogenic emission inventories in China: a review, *National Science Review*, 4, 834-866, 2017a.

887 Li, M., Zhang, Q., Kurokawa, J.-i., Woo, J.-H., He, K., Lu, Z., Ohara, T., Song, Y., Streets, D. G., and
888 Carmichael, G. R.: MIX: a mosaic Asian anthropogenic emission inventory under the international
889 collaboration framework of the MICS-Asia and HTAP, *Atmospheric Chemistry and Physics*, 17,
890 935-963, 2017b.

891 Liu, J., Strode, S. A., Liang, Q., Oman, L. D., Colarco, P. R., Fleming, E. L., Manyin, M. E., Douglass, A.
892 R., Ziemke, J. R., and Lamsal, L. N.: Change in tropospheric ozone in the recent decades and its
893 contribution to global total ozone, *Journal of Geophysical Research: Atmospheres*, 127,
894 e2022JD037170, 2022.

895 Lu, X., Zhang, L., Wang, X., Gao, M., Li, K., Zhang, Y., Yue, X., and Zhang, Y.: Rapid increases in
896 warm-season surface ozone and resulting health impact in China since 2013, *Environmental*
897 *Science & Technology Letters*, 7, 240-247, 2020.

898 Lu, X., Hong, J., Zhang, L., Cooper, O. R., Schultz, M. G., Xu, X., Wang, T., Gao, M., Zhao, Y., and
899 Zhang, Y.: Severe surface ozone pollution in China: a global perspective, *Environmental Science &*
900 *Technology Letters*, 5, 487-494, 2018.

901 Mallard, M. S., Spero, T. L., and Taylor, S. M.: Examining WRF's sensitivity to contemporary land-
902 use datasets across the contiguous United States Using Dynamical Downscaling, *Journal of applied*
903 *meteorology and climatology*, 57, 2561-2583, 2018.

904 Malley, C. S., Henze, D. K., Kuylenstierna, J. C., Vallack, H. W., Davila, Y., Anenberg, S. C., Turner, M.
905 C., and Ashmore, M. R.: Updated global estimates of respiratory mortality in adults \geq 30 years of
906 age attributable to long-term ozone exposure, *Environmental health perspectives*, 125, 087021,
907 2017.

908 Mao, J., Fan, S., Jacob, D. J., and Travis, K. R.: Radical loss in the atmosphere from Cu-Fe redox
909 coupling in aerosols, *Atmospheric Chemistry and Physics*, 13, 509-519, 2013.

910 Mao, J., Li, L., Li, J., Sulaymon, I. D., Xiong, K., Wang, K., Zhu, J., Chen, G., Ye, F., and Zhang, N.:
911 Evaluation of long-term modeling fine particulate matter and ozone in China during 2013–2019,
912 *Frontiers in Environmental Science*, 10, 872249, 2022a.

913 Mao, M., Rao, L., Jiang, H., He, S., and Zhang, X.: Air pollutants in metropolises of eastern coastal
914 China, *International Journal of Environmental Research and Public Health*, 19, 15332, 2022b.

915 Monks, P. S., Archibald, A., Colette, A., Cooper, O., Coyle, M., Derwent, R., Fowler, D., Granier, C.,
916 Law, K. S., and Mills, G.: Tropospheric ozone and its precursors from the urban to the global scale
917 from air quality to short-lived climate forcer, *Atmospheric chemistry and physics*, 15, 8889-8973,
918 2015.

919 Ni, R., Lin, J., Yan, Y., and Lin, W.: Foreign and domestic contributions to springtime ozone over
920 China, *Atmospheric Chemistry and Physics*, 18, 11447-11469, 2018.

921 Park, R. J., Jacob, D. J., Field, B. D., Yantosca, R. M., and Chin, M.: Natural and transboundary
922 pollution influences on sulfate-nitrate-ammonium aerosols in the United States: Implications for
923 policy, *Journal of Geophysical Research: Atmospheres*, 109, 2004.

924 Parrella, J., Jacob, D., Liang, Q., Zhang, Y., Mickley, L., Miller, B., Evans, M., Yang, X., Pyle, J., and
925 Theys, N.: Tropospheric bromine chemistry: implications for present and pre-industrial ozone and
926 mercury, *Atmospheric Chemistry and Physics*, 12, 6723-6740, 2012.

927 Sahu, S. K., Liu, S., Liu, S., Ding, D., and Xing, J.: Ozone pollution in China: Background and
928 transboundary contributions to ozone concentration & related health effects across the country,
929 *Science of the Total Environment*, 761, 144131, 2021.

930 Shen, C., Shen, A., Cui, Y., Chen, X., Liu, Y., Fan, Q., Chan, P., Tian, C., Wang, C., and Lan, J.:
931 Spatializing the roughness length of heterogeneous urban underlying surfaces to improve the
932 WRF simulation-part 1: A review of morphological methods and model evaluation, *Atmospheric
933 Environment*, 270, 118874, 2022.

934 Shen, Y., Liu, J., Chen, Z., Yang, M., Shu, L., Gai, C., and Jiang, Y.: Influence of wind flows on surface
935 O₃ variation over a Coastal Province in Southeast China, *Atmosphere*, 15, 262, 2024.

936 Siewert, J. and Kroszczynski, K.: Evaluation of high-resolution land cover geographical data for the
937 WRF model simulations, *Remote Sensing*, 15, 2389, 2023.

938 Solazzo, E., Bianconi, R., Vautard, R., Appel, K. W., Moran, M. D., Hogrefe, C., Bessagnet, B., Brandt,
939 J., Christensen, J. H., Chemel, C., Coll, I., Denier van der Gon, H., Ferreira, J., Forkel, R., Francis, X. V.,
940 Grell, G., Grossi, P., Hansen, A. B., Jeričević, A., Kraljević, L., Miranda, A. I., Nopmongkol, U., Pirovano,
941 G., Prank, M., Riccio, A., Sartelet, K. N., Schaap, M., Silver, J. D., Sokhi, R. S., Vira, J., Werhahn, J.,
942 Wolke, R., Yarwood, G., Zhang, J., Rao, S. T., and Galmarini, S.: Model evaluation and ensemble
943 modelling of surface-level ozone in Europe and North America in the context of AQMEII,
944 *Atmospheric Environment*, 53, 60-74, <https://doi.org/10.1016/j.atmosenv.2012.01.003>, 2012.

945 Tarasick, D., Galbally, I. E., Cooper, O. R., Schultz, M. G., Ancellet, G., Leblanc, T., Wallington, T. J.,
946 Ziemke, J., Liu, X., and Steinbacher, M.: Tropospheric Ozone Assessment Report: Tropospheric
947 ozone from 1877 to 2016, observed levels, trends and uncertainties, *Elem Sci Anth*, 7, 39, 2019.

948 Wang, K., Tong, Y., Gao, J., Gao, C., Wu, K., Yue, T., Qin, S., and Wang, C.: Impacts of LULC, FDDA,
949 Topo-wind and UCM schemes on WRF-CMAQ over the Beijing-Tianjin-Hebei region, China,
950 *Atmospheric Pollution Research*, 12, 292-304, 2021a.

951 Wang, N., Huang, X., Xu, J., Wang, T., Tan, Z.-m., and Ding, A.: Typhoon-boosted biogenic emission

952 aggravates cross-regional ozone pollution in China, *Science Advances*, 8, eabl6166, 2022.

953 Wang, N., Lyu, X., Deng, X., Huang, X., Jiang, F., and Ding, A.: Aggravating O₃ pollution due to
954 NO_x emission control in eastern China, *Science of the Total Environment*, 677, 732-744, 2019.

955 Wang, N., Du, Y., Chen, D., Meng, H., Chen, X., Zhou, L., Shi, G., Zhan, Y., Feng, M., and Li, W.:
956 Spatial disparities of ozone pollution in the Sichuan Basin spurred by extreme, hot weather,
957 *Atmospheric Chemistry and Physics*, 24, 3029-3042, 2024.

958 Wang, N., Xu, J., Pei, C., Tang, R., Zhou, D., Chen, Y., Li, M., Deng, X., Deng, T., and Huang, X.: Air
959 quality during COVID-19 lockdown in the Yangtze River Delta and the Pearl River Delta: Two
960 different responsive mechanisms to emission reductions in China, *Environmental Science &
961 Technology*, 55, 5721-5730, 2021b.

962 Wang, T., Xue, L., Brimblecombe, P., Lam, Y. F., Li, L., and Zhang, L.: Ozone pollution in China: A
963 review of concentrations, meteorological influences, chemical precursors, and effects, *Science of
964 the Total Environment*, 575, 1582-1596, 2017.

965 Wang, Y., Logan, J. A., and Jacob, D. J.: Global simulation of tropospheric O₃-NO_x-hydrocarbon
966 chemistry: 2. Model evaluation and global ozone budget, *Journal of Geophysical Research:
967 Atmospheres*, 103, 10727-10755, 1998.

968 Wang, Y., Gao, W., Wang, S., Song, T., Gong, Z., Ji, D., Wang, L., Liu, Z., Tang, G., and Huo, Y.:
969 Contrasting trends of PM_{2.5} and surface-ozone concentrations in China from 2013 to 2017,
970 *National Science Review*, 7, 1331-1339, 2020.

971 WHO: Ambient air pollution: A global assessment of exposure and burden of disease, *Clean Air
972 Journal*, 26, 6-6, 2016.

973 Willmott, C. J.: On the validation of models, *Physical geography*, 2, 184-194, 1981.

974 Yahya, K., He, J., and Zhang, Y.: Multiyear applications of WRF/Chem over continental US: Model
975 evaluation, variation trend, and impacts of boundary conditions, *Journal of Geophysical Research:
976 Atmospheres*, 120, 12748-12777, 2015.

977 Yarwood, G., Jung, J., Whitten, G. Z., Heo, G., Mellberg, J., and Estes, M.: Updates to the Carbon
978 Bond mechanism for version 6 (CB6), 9th Annual CMAS Conference, Chapel Hill, NC, 11-13,

979 Zhang, J., Wei, Y., and Fang, Z.: Ozone pollution: a major health hazard worldwide, *Frontiers in
980 immunology*, 10, 2518, 2019a.

981 Zhang, Q., Zheng, Y., Tong, D., Shao, M., Wang, S., Zhang, Y., Xu, X., Wang, J., He, H., and Liu, W.:
982 Drivers of improved PM_{2.5} air quality in China from 2013 to 2017, *Proceedings of the National
983 Academy of Sciences*, 116, 24463-24469, 2019b.

984 Zhao, F., Liu, C., Hu, Q., Xia, C., Zhang, C., and Su, W.: High Spatial Resolution Ozone Profiles
985 Retrieved from the First Chinese Ultraviolet-Visible Hyperspectral Satellite Instrument, *Engineering*,
986 32, 106-115, 2024.

987 Zheng, B., Cheng, J., Geng, G., Wang, X., Li, M., Shi, Q., Qi, J., Lei, Y., Zhang, Q., and He, K.: Mapping
988 anthropogenic emissions in China at 1 km spatial resolution and its application in air quality
989 modeling, *Science Bulletin*, 66, 612-620, 2021.

990 Zhixuan, B.: Lhasa SWOP atmospheric composition comprehensive sounding data set (2019-2020),
991 National Tibetan Plateau Data Center [dataset], 10.11888/Atmos.tpd.c.300007, 2023.

992 Zhu, Q., Bi, J., Liu, X., Li, S., Wang, W., Zhao, Y., and Liu, Y.: Satellite-based long-term
993 spatiotemporal patterns of surface ozone concentrations in China: 2005-2019, *Environmental
994 health perspectives*, 130, 027004, 2022.

995 Zhu, Y., Liu, Y., Li, S., Wang, H., Lu, X., Wang, H., Shen, C., Chen, X., Chan, P., Shen, A., Wang, H.,

996 Jin, Y., Xu, Y., Fan, S., and Fan, Q.: Assessment of tropospheric ozone simulations in a regional
997 chemical transport model using GEOS-Chem outputs as chemical boundary conditions, *Sci Total*
998 *Environ*, 906, 167485, 10.1016/j.scitotenv.2023.167485, 2024.
999